

In this document, the reviewers' comments are in black, the authors responses are in red.

The authors thank the reviewers for their additional useful suggestions to improve the quality of our manuscript.

Referee Report #1

Thank you for your accommodations of my comments. The impact this manuscript can have is much increased with the addition of the new section, though in reality, the method of focus is likely to not be used without co-located sonic anemometers.

Comments on the new Section 4.1:

Why the Kristensen model? Do you use isotropic or anisotropic, horizontally-homogenous? What do other models look like? That fit doesn't look great, but maybe that's the best there is? What kind of sensitivity/variability and error are introduced based on the choice of model and parameters? What kind of spread in time scales do you get?

We agree with the reviewer that many different spectral models have been proposed in the literature. Many of these, however, have been developed assuming specific atmospheric stability conditions: Kaimal et al. (1972) developed a spectral model in the neutral limit; unstable conditions were assumed in the studies by Kaimal et al. (1976), Panosky (1978), Kaimal (1978), Højstrup (1981 and 1982); while Kaimal (1973) and Caughey (1977) proposed spectral models for stable conditions. The model proposed by Kristensen does not depend on specific stability conditions, which is a desirable condition considered that we are proposing the use of spectral models when co-located in-situ measurements (necessary to quantify atmospheric stability conditions) are not available. The Section in our manuscript includes several references to the papers where different spectral models have been proposed, and where the interested reader can find additional details. We have also included the following sentence to better clarify our choice: "We test the spectral model proposed by Kristensen (1989), which proposes expressions for both the cases of an isotropic and an anisotropic horizontally homogeneous flow, without assumptions on the stability condition".

In addition, the Kristensen model (with the parameters we used) has been chosen in similar applications in recent studies – Lothon et al. 2009 and Tontilla et al. 2015, already included as references in the Section of our manuscript.

Moreover, we don't think that the specific choice of the functional form for the fit introduces a large uncertainty in our calculations. In fact, we think that the amount of information that a spectral model fit provides could even somehow be considered excessive, as our approach only aims at the determination of the extension of the inertial sub-range of the turbulence spectrum. As a consequence, we are also exploring the use of a simplified technique to determine the extension of the inertial sub-range by performing a local regression of the experimental spectra from the lidar, but we think that this further extension of the proposed method is beyond the scope of the present manuscript (where the lidars are co-located with a met tower, and so the calculation of spectra is not strictly necessary) and will be proposed in an additional manuscript in preparation.

Regarding the spread in the time scales we get, we think that a comprehensive analysis of these results for the proposed approach will better fit a later study, when the absence of co-located in situ measurements makes the use of lidar spectra the only available approach. In any case, for this

analysis, in unstable conditions the first quartile of the distribution of the timescales is 52s, while the third quartile is 83s. In stable conditions, the first quartile of the distribution of the timescales is 25s, while the third quartile is 43s. At this stage, we think it is sufficient to report in the Section of the present manuscript the values of MAE and correlation coefficient for the results presented here (Figure 10), as these are the metrics mostly used for all the comparisons made throughout the manuscript.

Finally, the chosen model assumes an anisotropic horizontally homogeneous flow. We have included the following sentence in the presentation of the model in the Section: “ assuming an anisotropic horizontally homogeneous flow”.

Pages 5, line 5: what was the last date of data used?

Data from the Halo lidar have been used until 16 April 2015 (as stated in the paragraph).

Figure 6 caption: misspelling "variability"

Corrected.

Page 14, line 9: "likely contributes an additional error for this lidar"

Corrected.

Page 14 line 17: "the inherent uncertainty in the sonic anemometers' retrievals of ϵ "

Corrected.

Page 17 line 5: spectral models can be fit

Corrected.

Add theoretical slope line to new Fig 9

The line has been added to the plot and the caption changed accordingly.

Referee Report #2

The authors have clearly made significant changes to the manuscript in response to concerns initially raised, including the addition of another section to further the applicability of the technique and results presented here. All of my initial concerns have been sufficiently addressed, and I recommend that this article be accepted pending some technical corrections on the new section.

- a) Eqs. 4 & 15: Modify these equations slightly to reflect the fact that the reported MAE values are %'s, as that is what is mostly used in the manuscript.

The equations now include a “ $\cdot 100$ ” term to show that the values are %'s.

- b) Throughout manuscript: Please be consistent on whether MAE is being reported as a % (Table 2, Figure 6, most of manuscript) or as a fraction (p. 6 l. 25, Figure 5) so that the values are directly comparable with each other.

MAE is now always reported as %. Figure 5 has been changed accordingly.

- c) Figure 9: Add units to the y-axis.

Added.

Estimation of turbulence dissipation rate and its variability from sonic anemometer and wind Doppler lidar during the XPIA field campaign

Nicola Bodini¹, Julie K. Lundquist^{1,2}, and Rob K. Newsom³

¹Department of Atmospheric and Oceanic Sciences, University of Colorado Boulder, Boulder, Colorado, USA

²National Renewable Energy Laboratory, Golden, Colorado, USA

³Pacific Northwest National Laboratory, Richland, Washington, USA

Correspondence to: Nicola Bodini (nicola.bodini@colorado.edu)

Abstract. Despite turbulence being a fundamental transport process in the boundary layer, the capability of current numerical models to represent it is undermined by the limits of the adopted assumptions, notably that of local equilibrium. Here we leverage the potential of extensive observations in determining the variability of turbulence dissipation rate (ϵ). These observations can provide insights towards the understanding of the scales at which the major assumption of local equilibrium between generation and dissipation of turbulence is invalid. Typically, observations of ϵ require time- and labor-intensive measurements from sonic and/or hot-wire anemometers. We explore the capability of wind Doppler lidars to provide measurements of ϵ . We refine and extend an existing method to accommodate different atmospheric stability conditions. To validate our approach, we estimate ϵ from four wind Doppler lidars during the 3-month XPIA campaign at the Boulder Atmospheric Observatory (Colorado), and we assess the uncertainty of the proposed method by data inter-comparison with sonic anemometer measurements of ϵ . Our analysis of this extensive dataset provides understanding of the climatology of turbulence dissipation over the course of the campaign. Further, the variability of ϵ with atmospheric stability, height, and wind speed is also assessed. Finally, we present how ϵ increases as nocturnal turbulence is generated during low-level jet events.

1 Introduction

Turbulence within the atmospheric boundary layer is critically important to transfer heat, momentum and moisture between the surface and the upper atmosphere (Sobel and Neelin, 2006). Hence, global and regional models need an accurate representation of turbulence to produce precise atmospheric predictions of winds, temperature and moisture in the boundary layer. An accurate forecast of these quantities has a critical impact on a variety of socio-economic activities, such as pollutant dispersion and air quality forecasting (Huang et al., 2013) and forest fires prediction and management (Coen et al., 2013). Wind energy production is also highly affected by turbulence in the boundary layer, as a lower power is generated when turbulence intensity is high (Wharton and Lundquist, 2012), and turbulence also reduces the lifetime of wind turbines (Kelley et al., 2006).

The production of turbulence kinetic energy in the boundary layer mainly takes place at large scales (Tennekes and Lumley, 1972). These large eddies then decay in smaller and smaller eddies through a "turbulence energy cascade" in the inertial

sub-range (Kolmogorov, 1941), until the length scales are small enough that molecular diffusion is capable of dissipating the kinetic energy into heat in the viscous sub-range. Current models assume that the generation of turbulence within a grid cell (local production) is balanced by the dissipation ϵ of turbulence kinetic energy in the same grid cell (local dissipation). This assumption of local equilibrium is appropriate for stationary and homogeneous flow (Albertson et al., 1997), and therefore it can be applied at coarse scales (Lundquist and Chan, 2007; Mirocha et al., 2010). However, at finer scales, the fundamental assumptions of turbulence closures are broken (Nakanishi and Niino, 2006; Hong and Dudhia, 2012). Therefore, when using models at fine horizontal resolution, the assumption of local equilibrium between generation and dissipation of turbulence is not valid anymore: turbulence produced in one grid cell can be advected downwind before being dissipated.

Hence, improved turbulence parametrizations are crucially needed to refine the accuracy of model results at fine horizontal scales. Yang et al. (2017) showed that, when testing the turbine-height wind speed sensitivity to different parameters in the Mellor–Yamada–Nakanishi–Niino (MYNN) planetary boundary-layer scheme (Nakanishi and Niino, 2009) and the MM5 surface-layer scheme (Grell et al., 1994) of the Weather Research and Forecasting model (Skamarock et al., 2005) in a complex terrain region, roughly half of the wind speed variance was due to the accuracy of the parametrization of the turbulence dissipation rate. ϵ also controls the evolution of several boundary layer processes, such as cyclone formation and dissipation (Zhang et al., 2009), the formation of frontal structures (Chapman and Browning, 2001; Piper and Lundquist, 2004), and the flow in urban areas and other canopies (Baik and Kim, 1999; Lundquist and Chan, 2007). Moreover, dissipation in aircraft vortices has a primary importance in aviation meteorology and air-traffic control (Gerz et al., 2005). Therefore, a correct representation of ϵ would improve the quality of numerical weather prediction. However, in order to improve turbulence parameterizations, the spatio-temporal variability of ϵ in the boundary layer needs to be studied in detail, as well as the dependence of ϵ with atmospheric stability, orography, and turbulence itself.

Estimates of turbulence dissipation rate have been calculated from sonic anemometers on meteorological towers in the past (Champagne et al., 1977; Muñoz-Esparza et al., 2017) and hot-wire anemometers suspended on tethered lifting systems (Frehlich et al., 2006; Lundquist and Bariteau, 2014) with the inertial sub-range energy spectrum method (Oncley et al., 1996) and the second-order structure function method (Frehlich and Sharman, 2004). Wind profiling radars have also been used to estimate ϵ (McCaffrey et al., 2017a), with the spectral width method. Wind Doppler lidars can also provide an extensive network of measurements of ϵ at different locations and at heights which are not accessible to traditional mast measurements. Four main methods are currently known to derive ϵ from lidar measurements, depending on the lidar scanning mode and measurement frequency: width of the Doppler spectra (Smalikho, 1995; Banakh et al., 1995), line-of-sight velocity spectrum (Banakh et al., 1995; Drobinski et al., 2000; O’Connor et al., 2010), line-of-sight velocity longitudinal structure function (Frehlich, 1994; Banakh and Smalikho, 1997; Smalikho et al., 2005), and line-of-sight velocity azimuthal structure function (Banakh et al., 1996; Frehlich et al., 2006).

In this study, we prove the capability of wind Doppler lidars to provide precise estimates of ϵ by refining the approach proposed in O’Connor et al. (2010) to estimate ϵ from lidar line-of-sight velocity spectra. We assess the uncertainty of this method, and present an extensive analysis of the variability of ϵ in the atmospheric boundary layer. We estimate turbulence dissipation rate from the 3-month period of the eXperimental Planetary boundary layer Instrumentation Assessment (XPIA) field campaign

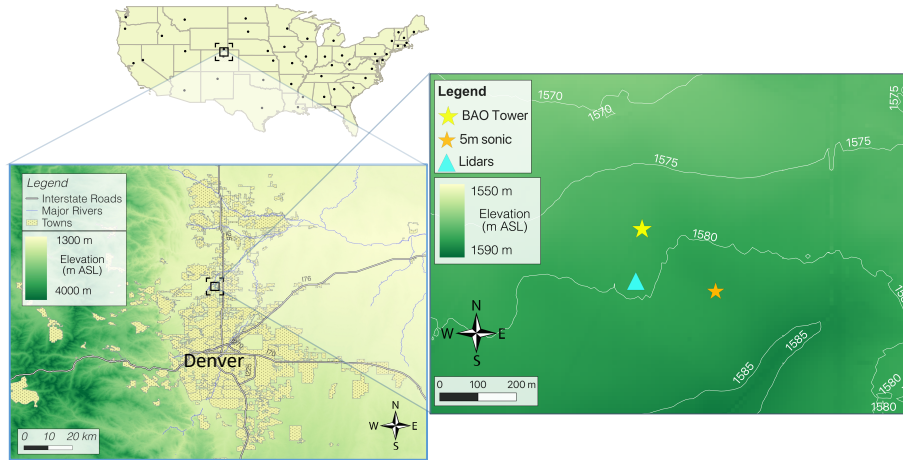


Figure 1. Map of the topography of the region where the XPIA field campaign took place. Contours in the right panel show elevation in m ASL.

(Lundquist et al., 2017), described in Section 2, from sonic anemometers and vertical profiling lidars, with the approach summarized in Section 3. The refinement of the method to derive ϵ from lidar to accommodate different stability conditions, and the quantification of its uncertainty are presented in Section 4. In Section 5 we assess the variability of ϵ with atmospheric stability, wind speed, and height, thus creating a climatology of turbulence dissipation. We finally focus, as a case study, on

5 how turbulence dissipation rate varies during a nocturnal low-level jet event.

2 Data

To analyze the variability of turbulence dissipation rate, we use data from the meteorological tower and wind Doppler lidars deployed during the XPIA field campaign, summarized in Lundquist et al. (2017). The XPIA campaign, which took place at the Boulder Atmospheric Observatory (BAO) in northern Colorado between 2 March and 31 May 2015, was designed to

10 explore the capabilities of multiple instruments to characterize different flow conditions in the boundary layer. As shown in the map in Figure 1, the region of the XPIA campaign is characterized by relatively flat terrain, with a few gentle hills south of the meteorological tower. The average elevation of the area is 1,584 MSL. Grass and low-crops fields surround the observatory, with some scattered trees and compact buildings.

2.1 Meteorological tower measurements

- 15 During XPIA, the 300-m BAO meteorological tower (Kaimal and Gaynor, 1983) had two 3D sonic anemometers (Campbell CSAT3) at each of six levels (50, 100, 150, 200, 250, and 300 m AGL), providing measurements with a frequency of 20Hz. The measurement accuracy was generally less than $1 \cdot 10^{-3} \text{ m s}^{-1}$ in the horizontal and $5 \cdot 10^{-4} \text{ m s}^{-1}$ in the vertical. At each level, the two sonic anemometers were mounted pointing northwest (334°) and southeast (154°). In order to avoid tower

wake effects, data from the northwest sonics are discarded when the wind direction was between 111° and 197° , while wind directions between 299° and 20° exclude data recorded by the southeast sonic (McCaffrey et al., 2017b). Data have been tilt-corrected according to the planar fit method described in Wilczak et al. (2001). An additional sonic anemometer was mounted on a 5-m AGL surface flux station located 200m south-west of the BAO tower over natural arid grassland. The sonic anemometer (Campbell CSAT3A) at this location operated with a frequency of 10Hz.

We quantify atmospheric stability from the 5-m tower data in terms of the Obukhov length L , defined as:

$$L = -\frac{\overline{\theta_v} \cdot u_*^3}{k \cdot g \cdot \overline{w'\theta_v'}} \quad (1)$$

where θ_v is the virtual potential temperature (K), calculated from the sonic anemometer virtual temperature data T_v and the measured pressure p as $\theta_v = T_v \left(\frac{p_0}{p}\right)^{R/c_p}$ with $p_0 = 1000$ hPa, and $R/c_p \approx 0.286$; $k = 0.4$ is the von Kármán constant; $g = 9.81$ m s $^{-2}$ is the gravity acceleration; $u_* = (\overline{u'w'^2} + \overline{v'w'^2})^{1/4}$ is the friction velocity (m s $^{-1}$); and $\overline{w'\theta_v'}$ is the kinematic sensible heat flux (Wm $^{-2}$). The turbulent quantities have been separated in average and fluctuating parts using the Reynolds decomposition with an averaging time of 30 minutes. This time scale is a common choice (De Franceschi and Zardi, 2003; Babić et al., 2012) when studying boundary layer processes, since it is generally longer than the turbulence time scales, but also shorter than the mean flow unsteadiness time-scales. For atmospheric stability, we classify neutral conditions as $L \leq -500$ m and $L > 500$ m; unstable conditions as $-500\text{m} < L \leq 0\text{m}$; and stable conditions as $0\text{m} < L \leq 500\text{m}$ (Muñoz-Esparza et al., 2012). Neutral conditions were rarely detected (less than 5% of the times) during the period of the campaign.

At the base of the BAO tower, a tipping-bucket rain gauge was used to measure precipitation. We have excluded from our analysis the times within one hour from precipitation events ($\sim 8\%$ of the times), as during these cases the measurement accuracy of both sonic anemometers and wind Doppler lidars drops.

2.2 Wind Doppler lidar measurements

Several vertical profiling and scanning wind Doppler lidars were deployed at XPIA. In this study, we focus on three vertical profiling lidars and one scanning lidar mainly used in vertical staring mode. All these instruments were co-located approximately 100m south of the BAO tower (Figure 1).

A WINDCUBE version 2 (v2) profiling lidar was deployed by the University of Colorado Boulder from 12 March to 8 June 2015. This lidar samples line-of-sight velocity in four cardinal directions with a nominal 28° zenith angle, followed by a fifth vertical beam. Range gates were centered on 40, 50, 60, 80, 100, 120, 140, 150, 160, 180, and 200m AGL. The retrieval of the actual wind speed from this measurement approach assumes horizontal homogeneity across the cone defined by the laser beams during the ~ 4 s required to complete a sequence of measurements across the five beams.

Two WINDCUBE version 1 (v1) profiling lidars (Aitken et al., 2012; Rhodes and Lundquist, 2013) were deployed by the University of Colorado Boulder and the National Center for Atmospheric Research from 1 and 4 March 2015 past the end of the experiment. These instruments measure line-of-sight velocity in four cardinal directions (nominal 28° zenith angle), with a range resolution of 20m, from 40 to 220 m AGL. The assumption of horizontal homogeneity of the flow in the sampling volume

Table 1. Main technical specifications of the lidars at XPIA used in this study.

	WINDCUBE v2	WINDCUBE v1 (61 & 68)	Halo Streamline
Wavelength	1.54 μm	1.54 μm	1.548 μm
Receiver bandwidth	± 57.5 MHz	± 55 MHz	± 25 MHz
Nyquist velocity (B)	± 44 m s^{-1}	± 42.3 m s^{-1}	± 19.4 m s^{-1}
Signal spectral width ($\Delta\nu$)	2.65 m s^{-1}	3.39 m s^{-1}	1.5 m s^{-1}
Pulses averaged (n)	20000	10000	20000
Points per range gate (M)	32	25	10
Range-gate resolution	10 – 20 m	20 m	30 m
Minimum range gate	40 m	40 m	15 m
Number of range gates	11	10	200
Pulse width	175 ns	200 ns	150 ns
Time resolution	~ 1 Hz	~ 1 Hz	~ 1 Hz

is again necessary to retrieve the actual wind vector. These instruments will be identified in the remainder of the analysis with their serial numbers, 61 and 68.

Finally, a Halo Photonics Streamline Doppler scanning lidar (Pearson et al., 2009) from the U.S. Department of Energy Office of Science Atmospheric Radiation Measurement program was deployed from 6 March to 16 April 2015. This lidar used a range gate resolution of 30m, with 200 total range gates. However, the maximum range gate with an acceptable number (> 30%) of valid measurements ($\text{SNR} > -20\text{dB}$) was at about 800m AGL. This scanning lidar was mainly used in a vertical staring mode. The scan strategy also included a 40-s plan-position-indicator (PPI) scan at an elevation angle of 60° once every 12min (from which the derivation of the horizontal wind speed is possible), a 10-min tower stare once per hour, and a target sector scan once per day to confirm heading relative to the tower (Newsom et al., 2017).

Table 1 includes the main technical characteristics of the three commercial lidar models considered in our analysis.

3 Methods to estimate turbulence dissipation rate ϵ

3.1 Turbulence dissipation from sonic anemometer

Sonic anemometers data can be used to calculate turbulence dissipation rate with two different methods: the inertial sub-range energy spectra method and the second-order structure function method. Muñoz-Esparza et al. (2017) analyzed data at XPIA and showed that the second-order structure function method has a lower error in estimating ϵ compared to the inertial sub-range energy spectra method, even when shorter overlapping temporal sub-windows are used to obtain a more regular pattern in the spectra. Therefore, we also apply the second-order structure function method to estimate ϵ from sonic anemometer measurements every 30s, for the 3-month period of XPIA.

According to Kolmogorov's hypothesis, within the inertial sub-range the velocity increments, expressed as second-order structure function D_U of the horizontal velocity U , can be related to ϵ as:

$$D_U(r) \equiv \langle [U(x+r) - U(x)]^2 \rangle = \frac{1}{a} \epsilon^{2/3} r^{2/3} \quad (2)$$

where $\langle \cdot \rangle$ denotes an ensemble average, and a is the Kolmogorov constant. We assume $a = 0.52$, which is consistent with the range of values present in the literature (Paquin and Pond, 1971; Sreenivasan, 1995). The spatial separations r , which must be within the inertial sub-range, can be expressed as temporal velocity increments by invoking Taylor's frozen turbulence hypothesis (Taylor, 1935), so that ϵ can be determined as:

$$\epsilon = \frac{1}{U\tau} [aD_U(\tau)]^{3/2} \quad (3)$$

where $D_U(\tau)$ is the second-order structure function of the horizontal velocity U calculated over temporal increments τ . For every ϵ calculation (i.e. every 30s), the second-order structure function was calculated with a 2-min window for τ , centered at the nominal time at which ϵ is calculated. Then, the fitting to the theoretical model only used the time range between $\tau = 0.1$ s and $\tau = 2$ s. Such a short temporal separation in the data is expected to lie well within the inertial sub-range, therefore excluding the undesired contributions from the outer scales which would undermine Kolmogorov's fundamental assumptions. Moreover, despite the reduced size of the chosen time range, the high temporal resolution of the sonic anemometers still guarantees an adequate number of data points to allow a robust estimation of the structure function. Data inspection confirms that the desired theoretical $\tau^{2/3}$ slope is observed in the chosen range for τ (example shown in the Supplement).

As already mentioned, data were excluded for wind directions waked by the tower. When neither of the two anemometers is affected by tower wakes, ϵ is defined as the average between the two independent values obtained from the two sonics at each height. To quantify the uncertainty in turbulence dissipation rate measurements from the sonic anemometers, we have compared ϵ from the two sonics at each level when neither one was influenced by the tower wake. For each tower boom direction (northwest and southeast), we calculate the median absolute error (MAE) between ϵ from the sonic anemometers mounted on the considered boom direction and the correspondent average value from the two sonics:

$$\text{MAE} = \text{median} \left(\frac{|\epsilon_{\text{single}} - \epsilon_{\text{average}}|}{\epsilon_{\text{average}}} \right) \cdot 100 \quad (4)$$

In calculating the error, we consider data from all heights, as no significant difference was noticed at different levels. For both the boom directions, we find very similar results, with ~~MAE = 0.19~~ MAE = 19%, which is reduced to ~~0.14~~ 14% when a 30-min running mean is applied to the ϵ time series. The distributions of the errors are included in the Supplementary Material. No bias was detected between the retrievals from the sonic anemometers on the two boom directions.

3.2 Dissipation from Doppler lidar

Wind Doppler lidars can provide a great improvement of our understanding of the variability of turbulence dissipation thanks to the ease of their deployment in different locations and the long measurement range allowed by several commercial models. To do so, robust methods to estimate ϵ with lidars are necessary, and their uncertainty has to be assessed. For this purpose, we

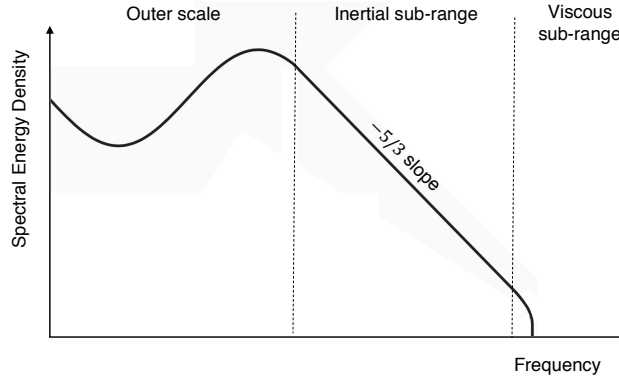


Figure 2. Turbulence energy spectrum according to Kolmogorov's hypothesis.

follow and refine the approach described in O'Connor et al. (2010) to estimate ϵ from vertical profiling lidars or scanning lidars used in vertical staring mode. For homogeneous and isotropic turbulence, within the inertial sub-range, the turbulent energy spectrum (Figure 2) can be expressed according to the Kolmogorov (1941) hypothesis in terms of wavenumber k as:

$$S(k) = a\epsilon^{2/3}k^{-5/3} \quad (5)$$

- 5 where $a \simeq 0.52$ is the one-dimensional Kolmogorov constant. The wavenumber k can be written in terms of a length scale $L = 2\pi/k$ by invoking Taylor's frozen turbulence hypothesis (Taylor, 1935). By integrating (5) over the wavenumber space, starting from the wavenumber k_1 correspondent to a single lidar sample, the variance σ_v^2 of the de-trended observed line-of-sight velocity from N samples can be obtained:

$$\sigma_v^2 = \int_{k_1}^{k_1} S(k)dk = -\frac{3}{2}a\epsilon^{2/3} \left(k_1^{-2/3} - k^{-2/3} \right) = \quad (6)$$

$$10 \quad = \frac{3a}{2} \left(\frac{\epsilon}{2\pi} \right)^{2/3} \left(L_N^{2/3} - L_1^{2/3} \right) \quad (7)$$

and therefore if the length scales are properly chosen (and consistent with how σ_v is computed) then ϵ can be calculated without the need of systematically computing turbulence energy spectra. In (7), the length scale L_1 for a single sample interval is given by:

$$L_1 = Ut + 2z \sin \left(\frac{\theta}{2} \right) \quad (8)$$

- 15 where U is the horizontal wind speed, t is the dwell time, θ the half-angle divergence of the lidar beam, and z the height AGL. Since Doppler lidars generally have a very small θ (< 0.1 mrad), the second term in (8) is typically negligible. For N samples, the length scale becomes $L_N = NUt$. For the WINDCUBE lidars, the variance of the observed line-of-sight velocity σ_v^2 can be calculated as average from all the beams. In doing so, we include turbulence contributions from both the horizontal and vertical dimensions, and we make the limiting (Kaimal et al., 1972; Mann, 1994) assumption of isotropic turbulence. For

the Halo Streamline lidar, which operated in a vertical stare mode, σ_v^2 is calculated from the vertically pointing beam, and therefore ϵ will strictly include turbulence contributions only in the vertical dimension, thus possibly determining different values compared to what is retrieved from the WINDCUBE lidars. Another difference due to the different scan patterns used by the considered lidars is related to the determination of the horizontal wind speed U . For the WINDCUBE lidars, U can be derived from the line-of-sight velocity measurements from the different beams, with the assumption of horizontal homogeneity of the flow over the probed volume. In the case of the Halo Streamline, no information about the horizontal wind can be derived from the measurements in the vertical staring mode, which only measures the vertical component of the wind speed. U is then retrieved from a sine-wave fitting from the VAD scans that are performed every 12min. The heights at which the measurements are taken during the tilted VAD scans are not the same as the heights sampled in the vertical staring mode. Therefore, for each considered level in the vertical staring mode, U is determined from a linear interpolation of the wind speed retrieved at the two closest heights during the VAD scans. Considerations about the error introduced by this procedure on the estimation of ϵ will be discussed in Section 4.

Lidar measurements are inherently affected by signal noise as well as possible variations of the aerosol fall speeds, which provide additional contributions to the observed variance. By assuming that the contribution of all atmospheric flows to the observed line-of-sight variance within the considered short time scales can be regarded as of turbulent nature, the variance σ_v^2 in (7) can be written as the sum of three different terms, which can be considered to be independent of one other (Doviak et al., 1993):

$$\sigma_v^2 = \sigma_w^2 + \sigma_e^2 + \sigma_d^2 \quad (9)$$

σ_w^2 is the desired net contribution from atmospheric turbulence at the scales that can be measured by the lidar (Brugger et al., 2016), from which the estimation of ϵ can be made. The additional contributions to the variance are due to the instrumental noise (σ_e^2) and the variation in the aerosol terminal fall speeds within the measurement volume from different sample intervals (σ_d^2), which however can safely be neglected since the particle fall speed is typically $< 1 \text{ cm s}^{-1}$. For a heterodyne Doppler lidar, Pearson et al. (2009) provides the following expression for the noise contribution to the variance, as a function of the signal-to-noise ratio (SNR):

$$\sigma_e^2 = \frac{\Delta\nu^2 \sqrt{8}}{\alpha N_p} \left(1 + \frac{\alpha}{\sqrt{2\pi}} \right)^2 \quad (10)$$

where N_p is the accumulated photon count:

$$N_p = \text{SNR} n M. \quad (11)$$

In this expression, n is the number of lidar pulses which are averaged to get a profile, and M is the number of points sampled within a single range gate to get a velocity estimate. α is the ratio of the lidar photon count to the speckle count (Rye, 1979):

$$\alpha = \frac{\text{SNR}}{\sqrt{2\pi}} \frac{B}{\Delta\nu} \quad (12)$$

where B is the bandwidth, equivalent to twice the Nyquist velocity, and $\Delta\nu$ is the signal spectral width. For the WINDCUBE lidars, σ_e^2 is calculated as average from all the beams.

The noise contribution to the observed variance determines an additional area below the turbulence spectrum in its high-frequency region (Frehlich, 2001) which, if not removed, would induce an overestimation of ϵ . Therefore, the turbulence dissipation rate can be estimated as:

$$\epsilon = 2\pi \left(\frac{2}{3a} \right)^{3/2} \left(\frac{\sigma_v^2 - \sigma_e^2}{L_N^{2/3} - L_1^{2/3}} \right)^{3/2} \quad (13)$$

- 5 This method relies on the assumption that both length scales L_1 and L_N are within the inertial sub-range. Therefore, the choice of the number of samples N to use should be carefully addressed, since only the turbulence contributions in the inertial sub-range should be included in the calculation. We discuss in detail this choice and its relationship with different atmospheric stability conditions and heights in the next section.

4 Error in turbulence dissipation rate estimates from lidar measurements

- 10 Although promising, the method to calculate ϵ from lidar data presented in the last section needs to be carefully analyzed in relation to its fundamental assumptions and its uncertainty, especially given the limited temporal resolution of lidar measurements. In this section we refine the method to derive ϵ from lidar data by discussing, in relationship with different heights and atmospheric conditions, the choice of the number of samples N to use for the calculation of the variance of the de-trended line-of-sight velocity and corresponding length scales. Moreover, we assess the uncertainty of this method by systematically
15 comparing ϵ values from lidar measurements with what is obtained from the sonic anemometers, and we discuss how the estimation error changes with height in the boundary layer.

- While the high temporal resolution of sonic anemometers facilitates the identification of sizable samples within the inertial sub-range, for lidars, the length of the samples used to estimate the variance of the line-of-sight velocity should be accurately chosen. In fact, the shorter the sampling time, the higher the measurement error in the estimate of the variance of line-of-sight
20 velocity would be, because of both higher measurement uncertainty which impacts its representativeness (Lenschow et al., 1994) and a higher relative contribution of the instrumental noise. According to the formulation in Lenschow et al. (2000), the measurement error $\Delta\sigma_w^2$ in the turbulence contribution to the observed variance σ_w^2 can be estimated as:

$$\Delta\sigma_w^2 \simeq \sigma_w^2 \sqrt{\frac{4\sigma_e^2}{N\sigma_w^2}} \quad (14)$$

- so it therefore decreases as the number of samples N increases, with the hypothesis that the noise contribution σ_e^2 to the
25 variance of each velocity sample used to estimate ϵ is similar to the ensemble mean error.

- On the other hand, if the sampling time is too long, the variance will incorporate undesired contributions from the large-scale processes, which would cause a severe underestimation of ϵ . Figure 3 shows how the estimated value of ϵ varies with the sample length used in the calculation, for a case using the WINDCUBE v2 data at 100m AGL. As long as the sample length stays within the inertial sub-range (up to ~ 45 s in the case shown), ϵ stays approximately constant. However, the estimate
30 of ϵ decreases by up to an order of magnitude when the contributions from the outer scales are erroneously included in the

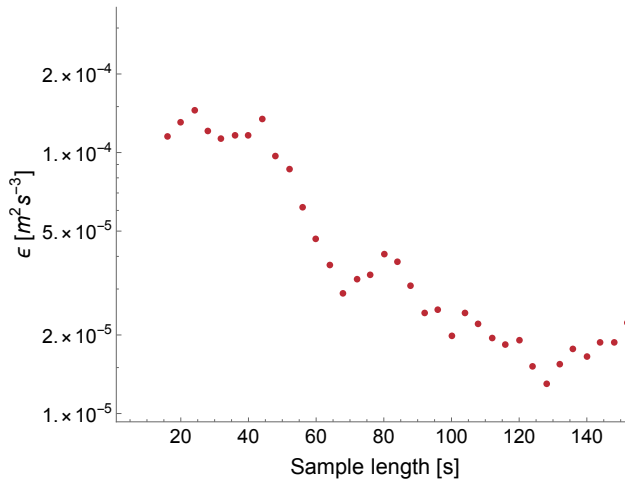


Figure 3. Example of the dependence of ϵ on the sample length used in the calculation. Data from the WINDCUBE v2 lidar at 100m AGL, 30 March 2015, 14:20 UTC.

calculation, which uses expressions that are valid strictly only within the inertial sub-range.

Moreover, since different atmospheric stability conditions are inherently characterized by different turbulence scales (Kaimal et al., 1972), the transition from the inertial sub-range to the outer scales occurs for different sample lengths, depending on the atmospheric stability. Figure 4 shows examples of turbulence spectra calculated over 15-min intervals for data measured by the WINDCUBE v2 lidar at 100m AGL in different stability conditions. For stable conditions (panel a), the transition from the inertial sub-range (which can be identified by comparing the slope of the spectrum with the theoretical $-5/3$ value shown by the dashed line) to the outer scales occurs at a higher frequency compared to the unstable case (panel b). Therefore, the choice of the number of samples N to use in the calculation should change accordingly. As a general rule, we expect shorter time scales to be adequate for stable conditions, when the turbulent eddies in the boundary layer are smaller, while longer scales would be more suitable during unstable conditions, characterized by larger convective eddies that can be fully captured only when using larger scales. Moreover, different altitudes can also impact the extension of the inertial sub-range, with a wider development expected at higher heights, as the integral length scale of turbulence increases (Wang et al., 2016).

To estimate the appropriate time scales which best balance these competing factors, we calculate ϵ , at each height from each of the considered lidars, using several values for the number of samples N used in the calculation. At the heights where there is correspondence between lidar and sonic anemometer measurements, we then compare the ϵ values from the lidars with the corresponding ϵ calculated at the meteorological tower. The estimates of ϵ from sonic anemometers and lidars have been calculated at slightly different time stamps, given the unavoidable difference in the nominal measurement time stamps of instruments operating with different temporal resolutions. Given the inherent turbulent nature of ϵ and its remarkable range of variability, the comparison between the time series from sonic anemometers and lidars could be flawed by the effect of the turbulent high-frequency variability of ϵ . Moreover, since this analysis is focused on the assessment of the appropriate time

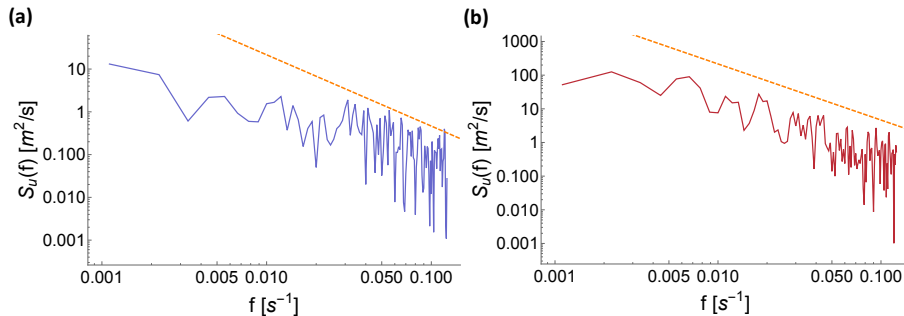


Figure 4. Turbulence energy spectrum for a stable case (panel a - 2 April 2015, 03:00 UTC), and an unstable case (panel b - 3 April 2015, 22:15 UTC), calculated from 15 minutes of data measured by the WINDCUBE v2 at 100m AGL. The dashed lines represent the theoretical $-5/3$ slope expected in the inertial sub-range. To calculate ϵ for these cases, the optimal sample length from comparison with the sonic anemometers corresponds to frequencies greater than 0.04s^{-1} for stable conditions, greater than 0.01s^{-1} for unstable conditions.

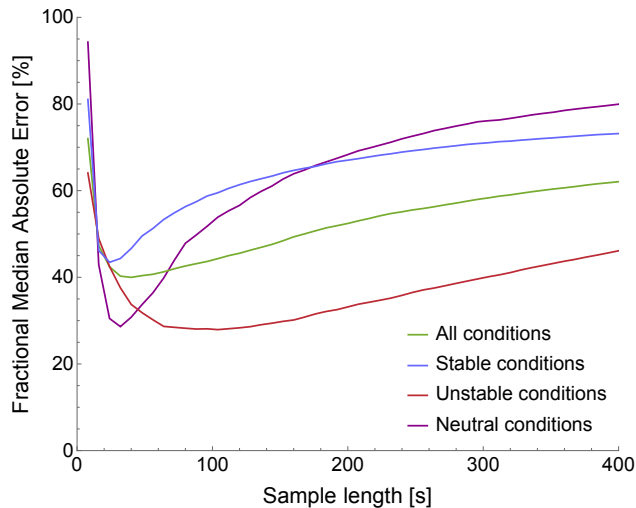


Figure 5. Median absolute error between ϵ estimates (smoothed with a 30-min running mean) from sonic anemometer and WINDCUBE v2 lidar data at 100m AGL during the whole period of the XPIA campaign, as a function of the sample length used to estimate ϵ from lidar data.

scales for different stability conditions, consistency with the time scale used to calculate turbulent fluxes for the determination of the Obukhov Length L is advisable. Therefore, a 30-min running mean is applied to the time series of ϵ from both sonic anemometers and lidars before comparing the estimates from the different instruments.

To quantify the difference between sonic and lidar estimates of ϵ , we use the median absolute error (MAE), defined as:

$$5 \quad \text{MAE} = \text{median} \left(\frac{|\epsilon_{\text{lidar}} - \epsilon_{\text{sonic}}|}{\epsilon_{\text{sonic}}} \right) \cdot 100 \quad (15)$$

The result of this comparison is reported in Figure 5, which shows how the MAE varies with the time scale (calculated as Nt , where t is the dwell time of the considered lidar) used to estimate ϵ for the WINDCUBE v2 lidar, for different atmospheric

Table 2. Time scales which minimize the median absolute error (MAE) in the comparison between ϵ from sonic anemometers and lidars at 100m AGL for stable and unstable conditions. Results for neutral conditions are not shown since these were rarely detected during the campaign.

	Stable conditions		Unstable conditions	
	Time scale	MAE	Time scale	MAE
WINDCUBE v2	24s	44%	88s	27%
WINDCUBE v1 - 61	24s	49%	96s	28%
WINDCUBE v1 - 68	32s	49%	72s	26%
Halo Streamline	28s	62%	73s	37%
Average	27s	51%	82s	29%

stability conditions, at 100m AGL. As the used sample length increases, the average error in ϵ estimated from lidar initially decreases from the high values related to the strong noise contribution at short time scales. Then, a minimum in the error is reached. As the size of the sample further increases, the average error rises again, due to the incorporation of undesired contributions from the outer scales. Moreover, as expected, the minimum error for stable (and neutral) conditions is found to be at shorter time scales than unstable conditions. Also, the minimum error in stable conditions is higher than minimum error for unstable conditions, since the need of using a shorter time scale implies a higher relative contribution of the instrumental noise to the error. The same qualitative pattern is found for all the considered lidars, at all heights. At each height, for each lidar and for each stability classification, we select the time scale that produces the lowest median absolute error compared to the sonic anemometer estimates of ϵ : this can be interpreted as the longest time scale that does not include substantial contributions from the undesired outer scales. Table 2 summarizes the selected time scales for the considered lidars for the different stability conditions (neutral conditions are not shown because they occurred less than 5% of the time), as well as the average from all the instruments, at 100m AGL. As expected, the larger eddies which characterize unstable conditions determine the need for a longer time scale to capture the influence of all the scales included in the inertial sub-range, while for stable conditions a shorter time scale is more appropriate. The median error is higher during stable conditions (average: MAE = 51%) compared to unstable conditions (average: MAE = 29%), as expected and as observed in other studies (Smalikho and Banakh, 2017).

Looking at the variability of the results with height, we find that the optimal time scales increase with height. At those heights < 300m AGL where lidar measurements do not match the level of any sonic anemometer on the meteorological tower, the adopted time scales are chosen as averages between the scales at the closest levels covered by sonics. For the Halo Streamline lidar, whose measurements are considered up to 800m AGL in this study, we determine the appropriate sample sizes by linearly extrapolating aloft, for each stability condition, the sequence of the chosen scales at the lower levels, where a comparison with the meteorological tower data is possible. The linear trend matches well the observed results up to 300m, with $R^2 > 0.9$ for all stability conditions (plot shown in the Supplementary Materials). Moreover, the rationality of the chosen

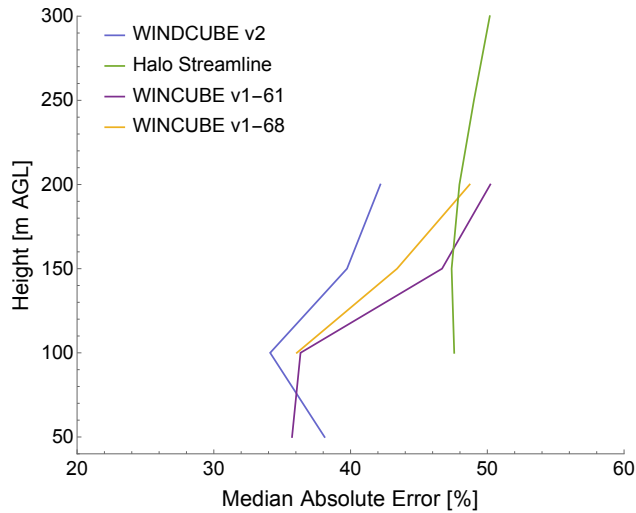


Figure 6. ~~Variability~~ Variability of the minimum median absolute error (calculated for the optimized number of samples at each height for each atmospheric stability conditions) between lidar and sonic anemometer estimates of ϵ (smoothed with a 30-min running mean) with height, for the four considered lidars.

scales at high altitudes has been confirmed after inspecting the extension of the inertial sub-range in turbulence spectra from the Halo Streamline lidar data (figure not shown).

Once the appropriate time scales have been identified at each height, considerations about how the error in lidar estimates of ϵ varies with height can be made. Figure 6 shows how the median absolute error between lidar and sonic estimates of ϵ changes with height, for all the levels at which sonic anemometers were mounted on the BAO tower. When a match between the height of lidar measurements and the level of the sonics was not present, the median error shown in the plot has been estimated as the average between the errors at the two closest lidar range gates. For the WINDCUBE v1-68, data at 50m AGL are not available because of measurement contamination due to hard strikes with the guy wires of the meteorological tower. The same issue invalidates measurements at 140m AGL from the WINDCUBE v1-61, so the comparison with the sonic anemometer at 150m AGL has been performed using only this lidar's data measured at 160m AGL. For the Halo Streamline, measurements below 105m AGL show a high percentage of low SNR data and therefore are not reported. For the WINDCUBE lidars, the median absolute error slightly increases with height, likely because of the severe reduction of the number of acceptable measurements at higher levels, and it always stays below 50%. For the Halo Streamline lidar, the median error stays almost constant in the considered portion of the boundary layer. It is reasonable to explain the higher error ($\sim +10\%$) of the Halo Streamline compared to the WINDCUBE lidars at 100m AGL as a consequence of the differences in the spatial dimensions that are samples by the two lidars. While the lidar beams of the WINDCUBE are tilted, and they therefore include turbulence contributions in the horizontal dimension (which is the only contribution considered in the determination of ϵ from the sonic anemometers), ϵ from the Halo Streamline is only retrieved using information from the vertically pointing beams. Moreover, the necessary approximations adopted in the determination of the horizontal velocity U for the Halo Streamline lidar, as explained

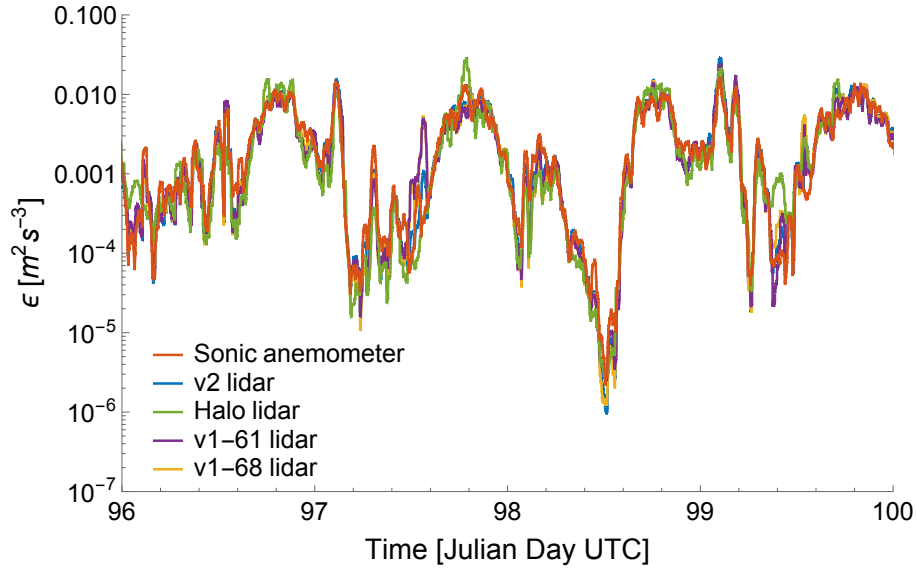


Figure 7. Time series from 6 April 2015 00 UTC to 10 April 2015 00 UTC comparing ϵ from sonic anemometers and all the considered lidars at 100m AGL. Data have been smoothed with a 30-min running mean.

in Section 3.2, likely ~~determine~~contributes an additional error ~~increase~~ for this lidar. However, the magnitude of this additional error due to the reduced frequency in determining U for the Halo Streamline is comparable with the additional uncertainty related to the drop of instrumental performance that the WINDCUBE show at higher levels. Therefore, the estimates of ϵ from the Halo Streamline can be considered physically robust in the lowest few hundred meters of the boundary layer.

- 5 Possible sources for the discrepancy found between ϵ from sonic anemometers and lidars might arise from the different temporal resolution and sampling volumes of the various instruments, as well as the 100m spatial separation between the lidar site and the BAO meteorological tower. In any case, given the wide range of variability of ϵ , which can span ~ 6 orders of magnitude during its typical diurnal cycle (Section 5), and the inherent uncertainty in ~~ϵ retrievals even from just~~ the sonic anemometers' retrievals of ϵ (Section 3.1), the obtained magnitudes of the error prove that the refined method to retrieve ϵ from
- 10 lidar measurements gives robust estimates of turbulence dissipation rate. The accommodation for different stability conditions in the choice of the time scales used in the method considerably reduces, especially for stable conditions, the magnitude of the errors (obtained through propagation of errors) found in the original study (O'Connor et al., 2010). To visualize the good agreement between sonic anemometer and lidar estimates of ϵ , Figure 7 shows the time series for a portion of the XPIA campaign, with values from all the considered instruments at 100m AGL. A clear diurnal pattern is revealed, with higher
- 15 values of turbulence dissipation during the day, and differences of several orders of magnitude between daytime and nighttime values of ϵ . These results will be explored in more detail in Section 5. A systematic comparison between ϵ estimates from sonic anemometers and the WINDCUBE v2 lidar at 100m AGL is shown by the density histograms in Figure 8, for the whole period of the XPIA campaign, for different stability conditions and smoothing. The coefficient of determinations R^2 are also reported

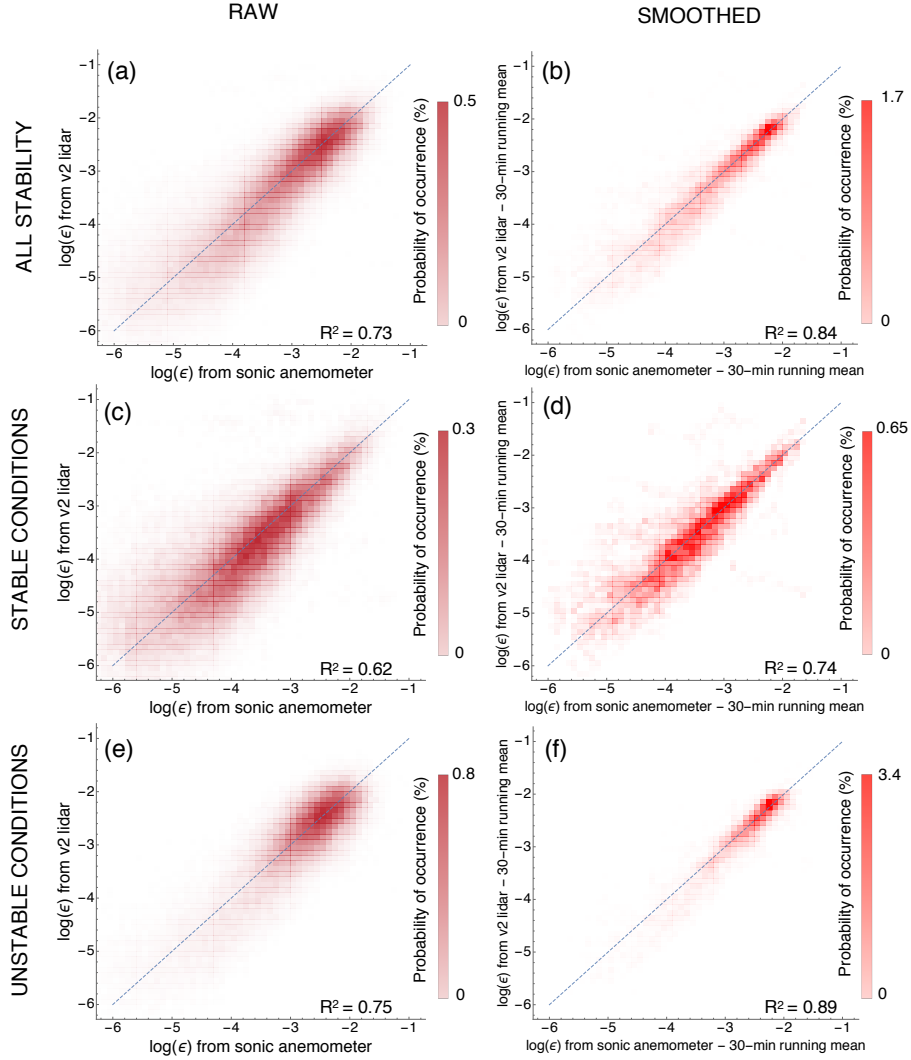


Figure 8. Correlation between ϵ values from sonic anemometer and WINDCUBE v2 lidar at 100m AGL for the whole period of the XPIA campaign, using the selected time scales for the estimation of ϵ from lidar data. The color scales represent the probability of occurrence in percentage, and the dark dashed lines show perfect correlation. (a) All stability conditions, raw data (MAE = 62%); (b) all stability conditions, 30-min running mean applied (MAE = 34%); (c) stable conditions, raw data (MAE = 67%); (d) stable conditions, 30-min running mean applied (MAE = 44%); (e) unstable conditions, raw data (MAE = 58%); (f) unstable conditions, 30-min running mean applied (MAE = 27%).

in the plots. The good agreement between data from sonic anemometer and lidars is confirmed, with unstable conditions showing a better performance ($R^2 = 0.89$ for the smoothed time series) compared to stable conditions ($R^2 = 0.74$). Moreover, the plots show the effect of the choice of applying the 30-min running mean before comparing ϵ values from the different instruments. In the figure, the panels on the left compare ϵ without any temporal filter (one value every ~ 4 s), while the panels

on the right show the comparison between time series after the 30-min running mean has been applied. The application of the 30-min running mean to the ϵ time series increases the correlation between the different time series. In any case, even for the raw time series, the values of the coefficient of determination are always greater than 0.6.

4.1 Determination of the optimal time scales to retrieve ϵ from lidars in absence of co-located sonic anemometers

- 5 The availability of multiple sonic anemometers co-located with the lidars at XPIA has allowed for a direct comparison between ϵ estimates from different instruments to determine the optimal length scales, in different stability conditions, to use when retrieving ϵ from Doppler lidar measurements. This approach does not require the direct calculation of spectra from the line-of-sight velocity measured by the lidars, and therefore it represents a time-efficient technique. However, the proposed method is only viable when sonic anemometers are deployed in the near vicinity of a lidar, and when measures of atmospheric stability
10 are available.

- When a comparison with sonic anemometer data is not possible, the appropriate time scale to use in the lidar retrieval of ϵ can be determined by finding the maximum wavelength within the inertial sub-range in the velocity spectra from the lidar measurements. To do so, spectral models can be ~~fitted~~ fit to the observed spectra. Several models have been proposed for turbulence spectra in different stability conditions (Kaimal et al., 1972; Panofsky, 1978; Olesen et al., 1984). We test the
15 spectral model proposed by Kristensen et al. (1989), which proposes expressions for both the cases of an isotropic and an anisotropic horizontally homogeneous flow, without assumptions on the stability condition. To validate our results and test this alternative approach to derive ϵ from lidar measurements, we use data from the Halo Streamline lidar to estimate the maximum wavelength λ_z within the inertial subrange. Since the Halo mainly operated in a vertical stare mode during XPIA, we consider the following expression for the turbulence spectrum of the vertical component of the wind speed, assuming an anisotropic
20 horizontally homogeneous flow:

$$S(k) = \frac{\sigma_z^2 l_z}{2\pi} \frac{1 + \frac{8}{3} \left(\frac{l_z k}{a(\mu)} \right)^{2\mu}}{\left[1 + \left(\frac{l_z k}{a(\mu)} \right)^{2\mu} \right]^{5/(6\mu)+1}} \quad (16)$$

- where k is the wavenumber, σ_z is the standard deviation of the vertical component of the wind speed used to compute the spectrum, l_z is the integral scale of the vertical velocity along the horizontal flow trajectory, and the parameter μ controls the curvature of the spectrum. We use $\mu = 1.5$, which provides a good match with our experimental spectra, as also found in
25 previous studies (Lothon et al., 2009; Tonttila et al., 2015). The parameter a can be expressed as a function of μ as:

$$a(\mu) = \pi \frac{\mu \Gamma\left(\frac{5}{6\mu}\right)}{\Gamma\left(\frac{1}{2\mu}\right) \Gamma\left(\frac{1}{3\mu}\right)} \quad (17)$$

We calculate spectra using 10-min consecutive data, and we fit the spectral model to the experimental data, leaving out frequencies greater than 0.2Hz, which are affected by instrumental noise (Frehlich, 2001), not modeled here. An example of a measured spectrum and the fit resulting from the model are shown in Figure 9. The transition wavelength λ_z between the

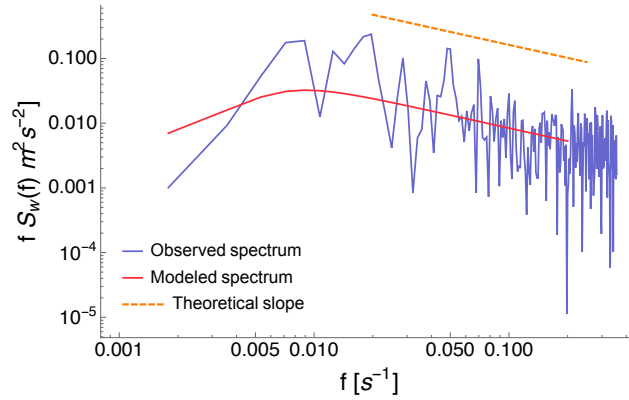


Figure 9. Example of power spectral density of the vertical component of the wind speed as measured by the Halo Streamline lidar on 11 March 2015 18:05 UTC. The red line represents the fit according to the spectral model from Eq. (16), the orange dotted line shows the theoretical slope.

inertial sub-range and the outer scales can be expressed as a function of the integral scale l_z and the parameter μ :

$$\lambda_z = \left[\frac{5}{3} \sqrt{\mu^2 + \frac{6}{5}\mu + 1} - \left(\frac{5}{3}\mu + 1 \right) \right]^{1/(2\mu)} \frac{2\pi}{a(\mu)} l_z \quad (18)$$

Following the approach in Tonttila et al. (2015), we estimate the timescale corresponding to this transition wavelength by dividing λ_z by the collocated wind speed derived from the closest PPI scan performed by the Halo Streamline lidar.

- 5 To compare the results from this approach with what we obtain from the comparison with dissipation rates from the sonic anemometer data, we apply this technique to the data from the Halo Streamline for the whole period of XPIA, and calculate the average timescales for different stability conditions at 100m AGL. We obtain an average time scale of 32s in stable conditions, and 73s in unstable conditions. Both these values compare well with what is found with the more time-efficient comparison with the sonic anemometer retrievals (values in Table 2), thus confirming that the use of spectral models can be considered a
- 10 valid alternative for the determination of the optimal sample lengths to retrieve ϵ from lidar data.

- The use of spectral models to determine the appropriate sample size to use when retrieving ϵ from lidars can also be applied when information about atmospheric stability are not available or accurate. In these cases, instead of calculating an average optimal sample size for each stability condition, an appropriate time scale can be determined at each time ϵ is retrieved from lidar measurements, from a single spectrum. We compare ϵ values from the sonic anemometers and from the Halo Streamline
- 15 lidar, with the optimal time scales obtained from both the proposed approaches (comparison with the sonic anemometer data and analysis of instantaneous spectra) in Figure 10, for the same time period shown in Figure 7. The use of spectral models to determine the extension of the inertial sub-range in the lidar spectra produces valid estimates of ϵ : for this case we obtain a $\text{MAE} = 0.40 = 40\%$, and a correlation coefficient $R^2 = 0.78$.

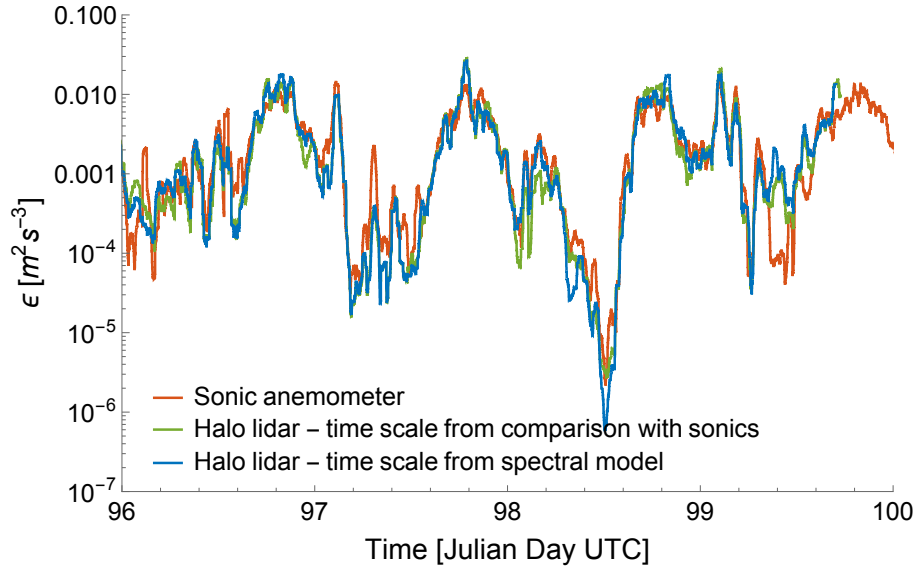


Figure 10. Time series from 6 April 2015 00 UTC to 10 April 2015 00 UTC comparing ϵ from sonic anemometers and the Halo Streamline lidars at 100m AGL, where the time scales for the lidars have been determined with both the proposed approaches (comparison with ϵ from sonic anemometers and fit with spectral models). Data have been smoothed with a 30-min running mean.

5 Variability of turbulence dissipation rate

Once the capability of the method to provide accurate estimates of ϵ from lidar data has been tested, the variability of turbulence in the boundary layer can be assessed, using data from the various instruments deployed at XPIA.

The time series of ϵ shown in the previous section revealed that, during the course of the day, ϵ changes by several orders of magnitude. To better explore this diurnal variability, Figure 11 shows the daily climatology of turbulence dissipation rate, calculated as median of the data from the sonic anemometer, WINDCUBE v2 lidar and Halo Streamline lidar. Plots for the two WINDCUBE v1 lidars are shown in the Supplementary Materials, and are similar to the results from the WINDCUBE v2. A general good agreement between the climatology from sonic anemometers and lidars can be observed. A definite diurnal pattern is evident from each panel. As expected, the mainly quiescent conditions at night determine low values of turbulence dissipation rate ($\epsilon \sim 10^{-5} - 10^{-4} \text{ m}^2 \text{ s}^{-3}$), while daytime convection increases the median turbulence dissipation in the boundary layer by several orders of magnitude ($\epsilon \sim 10^{-2} \text{ m}^2 \text{ s}^{-3}$). During nighttime, however, the median values of ϵ show more variability than during daytime conditions, as traces of intermittent bursts of ϵ can be detected in the climatology. We will investigate these changes in ϵ in more detail, by relating the variability of ϵ with wind speed, especially in the case of nocturnal low-level jets.

Also, the study of the climatology of ϵ can give insights on how ϵ changes with height. The analysis of the climatology from the sonic anemometers (right panel in Figure 11), which allow measurements of ϵ at 5m AGL, shows how ϵ is higher close to the surface throughout the day, while above 50m AGL the change of ϵ with height is less noticeable. A similar result can be found from lidars, which provide ϵ measurements starting at 40m AGL for the WINDCUBE v2, and 75m AGL for the Halo

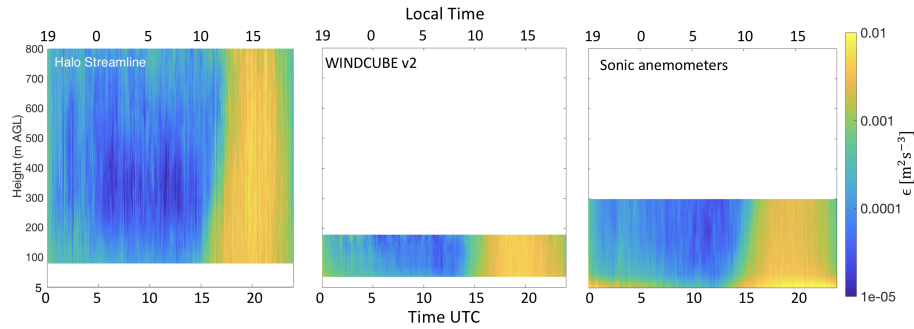


Figure 11. Daily climatology of turbulence dissipation rate derived from raw values from the Halo Streamline (left), the WINDCUBE v2 lidar (center), and sonic anemometers (right). Results from the two WINDCUBE v1s are included in the Supplementary Material.

Streamline, with reduced variability of ϵ with height in the majority of the sampled height range. The slight increase of ϵ above ~ 600 m AGL at night for the Halo Streamline lidar (left panel in Figure 11) can be explained as due to more random errors in the line-of-sight velocity measured by the lidar at high altitudes but also as effect of the higher frequency of good-quality measurements at higher levels during high wind speed events, which determine higher turbulence, as will be shown later in this section. A systematic analysis of how turbulence dissipation rate varies with height is shown in Figure 12. For each instrument, the percentage difference in ϵ is shown, and it is calculated by taking as reference value the ϵ value closest in time from the sonic anemometer at 5m AGL, so that a common reference level is identified for all the instruments. The continuous line in the plot shows the median value at each height, while the shaded band represents the 1st and 3rd quartiles of the data distribution. The plot confirms that turbulence dissipation rate shows most of its variability with height close to the surface, as also found by Balsley et al. (2006). A 75% decrease in the median ϵ value is observed moving from 5m AGL to 50m AGL for the sonic anemometer data. We expect this large reduction in ϵ to be due to a rapid decrease in shear production with height close to the surface, as it has been shown (Nilsson et al., 2016) that shear production has a strong connection with dissipation close to the surface. An additional increase of height determines a lower rate of average reduction of ϵ with height, with the median ϵ values for the sonics experiencing an additional 15% reduction (compared to the reference 5m AGL level) between 50m AGL and 300m AGL. Variations of comparable magnitude are also found for the lidar data, for both the WINDCUBE v2 and the Halo Streamline. In any case, the spread around the median value is quite extensive at all the considered heights for all the instruments.

The effect of different atmospheric stability conditions on turbulence dissipation can be investigated in more detail by relating ϵ with the correspondent Obukhov length (L) values, which is used here as a measurement of stability. Figure 13 shows the relationship between turbulence dissipation rate and the absolute value of L , for the sonic anemometers, the WINDCUBE v2, and the Halo Streamline, at 100m AGL. For each instrument, we sort ϵ based on L . Then, we sub-divide the ϵ data in correspondence of equally-spaced (in the logarithmic space) L bins. The median ϵ in each group is shown by the continuous line in the plot. The shaded area shows the range between the 1st and 3rd quartiles. Results from raw ϵ data (i.e. without the application of the 30-min running mean) are shown in the plot. However, no substantial differences arise from the use of

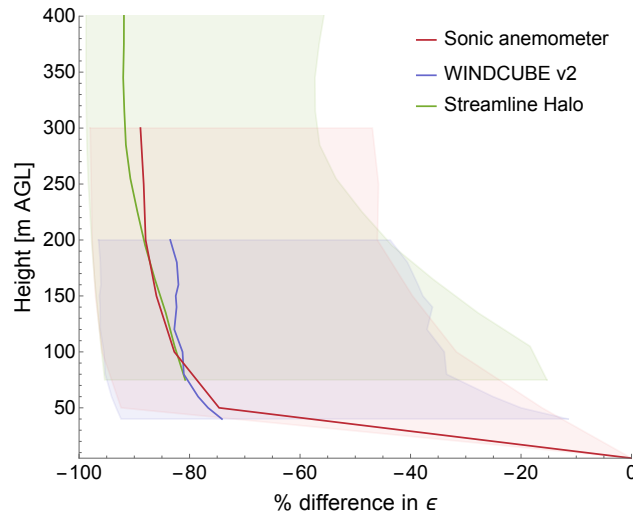


Figure 12. Turbulence dissipation rate (raw values) as a function of height for different instruments. The variability with height is expressed as percentage change assuming as reference level 5m AGL. The continuous line in the plot represents the median value for different instruments, while the shaded area creates a band corresponding to the 1st and 3rd quartiles of the values.

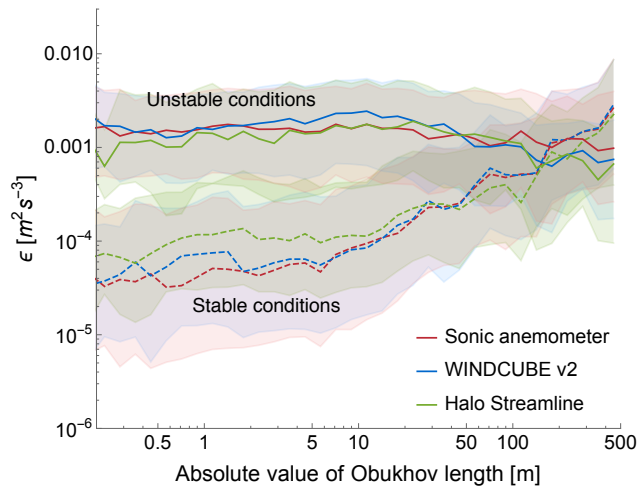


Figure 13. Turbulence dissipation rate (raw values at 100m AGL) as a function of the absolute value of the Obukhov Length L . The thick lines in the plot represent the median value for the different instruments, while the shaded area creates a band corresponding to the 1st and 3rd quartiles of the distributions. Continuous (dashed) lines for unstable (stable) conditions. Results from the two WINDCUBE v1s are included in the Supplementary Material.

the smoothed time series. The Supplementary Material includes the plot for the WINDCUBE v1s, which provide results very similar to what shown here. Different stability conditions systematically change the magnitude of turbulence dissipation rate,

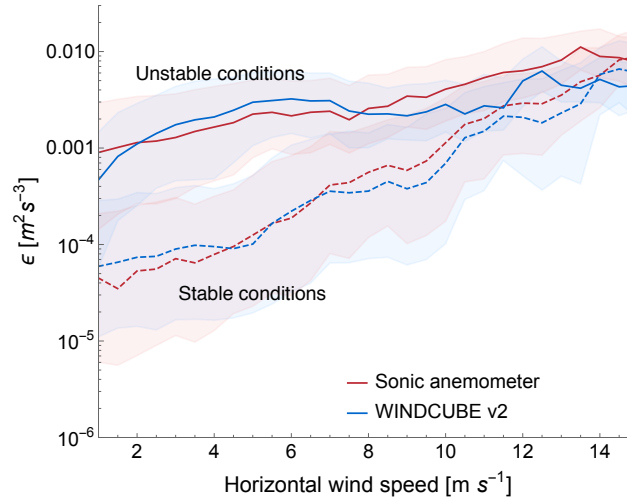


Figure 14. Turbulence dissipation rate (raw values) as a function of the 2-min average wind speed, as measured at 100m AGL. The thick lines in the plot represent the median value for the different instruments, while the shaded area creates a band corresponding to the 1st and 3rd quartiles of the distributions. Continuous (dashed) lines for unstable (stable) conditions. Results from the two WINDCUBE v1s are included in the Supplementary Material.

with median ϵ values during strong stable conditions ($L > 0\text{m}$) generally two orders of magnitude lower than what is found for strongly unstable conditions ($L < 0\text{m}$). Moreover, as the atmospheric stability conditions become less strong, with an increase in the absolute value of L , the median ϵ values tend to converge to a common value, with ϵ in stable conditions recording a higher increase compared to the change in ϵ for different values of L in unstable conditions. Results from neutral conditions

5 $|L| > 500\text{m}$ are not shown as they rarely occurred at the site during the field campaign.

Different wind speed regimes can also have a strong impact on the development and subsequent dissipation of turbulence. Figure 14 relates turbulence dissipation rate with 2-min average wind speed, for different stability conditions, at 100m AGL (results for the WINDCUBE v1s are included in the Supplementary Material as very similar to what is found for the v2). The same sampling technique described for Figure 13 to define median ϵ values, shown by the continuous line, has been applied

10 in this case. Data from the Halo Streamline are not included here since the reduced temporal availability of horizontal wind speed measurements (once every 12min) does not guarantee a precise estimation of the variability of ϵ with wind speed for this instrument. For both the sonic anemometer and the WINDCUBE v2 lidar data, a strong dependence of ϵ on wind speed can be observed. As wind speed increases, more turbulence is generated - and therefore dissipated - in the boundary layer. The median ϵ increases of 1-2 orders of magnitude as wind speed intensifies from 1 m s^{-1} to 15 m s^{-1} . This positive correlated trend

15 is found for both stable and unstable conditions, with ϵ in stable conditions being more subject to variations with wind speed compared to ϵ in unstable conditions. Also, the difference in ϵ during distinct stability conditions becomes less pronounced as the wind speed increases. Therefore, high wind speeds seem to determine strong turbulence - and turbulence dissipation - without any significant dependence on the stability condition.

5.1 Turbulence dissipation rate during nocturnal low-level jet events

The accurate numerical representation of nocturnal low-level jets has a crucial importance. In fact, this sudden increase of wind speed aloft at night has been shown to have a primary effect on turbulent transport (Prabha et al., 2007), clear-air turbulence (Banta et al., 2002), storm formation (Curtis and Panofsky, 1958), forest fire propagation (Barad, 1961), and wind energy resources (Vanderwende et al., 2015). In all these cases, turbulence represents an essential driving mechanism, and therefore turbulence dissipation needs to be represented with particular attention. During XPJA, nocturnal low-level jets have been observed several times (Lundquist et al., 2017). As case study, Figure 15 shows how wind speed, wind direction, and turbulence dissipation rate varied during the night between 6 - 7 April 2015, as measured by the Halo Streamline lidar. The analysis of the weather maps for this period reveals no frontal passage during the LLJ event, while a quasi-stationary front likely occurred at the end of the event (~ 23 LT), as also confirmed by the shift in wind direction during this period, as shown in Figure 15b. No precipitation was recorded; and the analysis of ceilometer data reveals clear sky. A considerable increase in wind speed (up to 14 m s^{-1} , Figure 15a) can be observed between 21 and 23 LT. In correspondence to this jet, turbulence dissipation rate (Figure 15c) increases by at least an order of magnitude throughout the considered vertical portion of the boundary layer, as a consequence of an increase in wind speed variance, as observed in previous studies (Banta et al., 2006). ϵ reaches values of $\sim 10^{-2} \text{ m}^2 \text{ s}^{-3}$ which are comparable to what is observed during daytime convection, as can be seen between 15 and 17 LT in the presented case. This abrupt increase of ϵ , which interrupts the normal decrease of ϵ due to the transition from daytime convection to nocturnal quiescence, can also clearly be detected in the time series shown in Figure 7. After the end of the low-level jet event, in combination with the development of the quasi-stationary front, the return to more quiescent conditions, typical of the nighttime stable boundary layer, causes a considerable reduction of turbulence dissipation rate. Therefore, the turbulence generated by the strong wind acceleration during nocturnal low-level jets can deeply modify the daytime climatology of ϵ , determining the temporary increases which have been detected in the analysis of the climatology in Figure 11.

6 Conclusions

Turbulence parametrizations currently used in numerical models have been proved (Yang et al., 2017) to have considerable limitations which undermine the quality of representations of processes in the atmospheric boundary layer. A crucial parameter in this regard is the turbulence dissipation rate (ϵ). Currently, most mesoscale planetary boundary layer models make the assumption of local equilibrium between production and dissipation of turbulence. In this study, we have demonstrated the value of observations from both in situ and remote sensing instruments in providing insights on the variability of turbulence dissipation rate, and we have assessed how ϵ changes with atmospheric stability, wind speed, and height in the boundary layer.

We have refined an approach to use wind Doppler lidars to quantify ϵ . Our analysis provides recommendations about the choice of the length of sample of lidar measurements to calculate ϵ . In fact, the properties of the turbulence energy spectra for different atmospheric stability conditions have to be taken into account to balance the competing needs of keeping the sampled scales within the inertial sub-range, while minimizing the impact of the instrumental noise. We found that longer time scales are appropriate for unstable conditions, while shorter scales should be used in stable cases. Also, the choice of the appropriate

sample size should consider the variability of turbulence spectra with height, with longer scales more suitable aloft. The choice of the appropriate time scales can be made by either comparing lidar estimates of ϵ with sonic anemometer data in different stability conditions and heights or by inspecting the properties of the turbulence spectra from lidar measurements with the use of spectral models.

5 We have tested our methodology by calculating ϵ from four wind Doppler lidars deployed during the XPIA field campaign at the Boulder Atmospheric Observatory in Spring 2015. We have systematically compared the lidar estimates of ϵ with reference data from sonic anemometer measurements to determine the appropriate time scales to use in the calculation. Considering that ϵ spans several orders of magnitude throughout its diurnal cycle, our results reveal good agreement between lidar and sonic anemometer estimates of ϵ , with median differences lower than 30% in unstable conditions, and lower than 50% in stable
10 conditions.

This analysis reveals that different stability conditions have a considerable impact on determining the magnitude of ϵ . This dual pattern determines the diurnal climatology of ϵ , with lower values during nighttime quiescent conditions and increased turbulence during the daytime convection, as would reasonably be expected. However, the general pattern of the climatology of ϵ strongly varies based on turbulence generation and dissipation due to the magnitude of wind speed. We have found that higher
15 wind speeds cause increased turbulence dissipation, with the gap between ϵ values in stable and unstable conditions becoming less pronounced as the wind speed increases. Therefore, important boundary layer processes such as nocturnal low-level jets can induce a substantial increase of ϵ at night, with values which can reach those of daytime convective turbulence. Finally, we have shown how most of the variability of ϵ occurs in the lowest part of the boundary layer, with a 75% reduction from 5m AGL to 50m AGL.

20 The results from this dataset represent a significant progress towards the full understanding of how turbulence dissipation varies in the boundary layer. The promising results of the method we propose to retrieve ϵ from lidar measurements make a considerable amount of data, measured in the recent years with vertical-profiling lidars, now potentially available to create an extensive database of turbulence dissipation rate for different atmospheric and topographic conditions. Wide deployments of lidars can in fact provide measurements in several different locations and at heights which are not accessible to traditional tower
25 measurements. Future work should include testing the capability of lidars to measure turbulence dissipation rate in complex terrain, with potential case studies including mountain waves phenomena and diurnal circulations, as well as during other specific boundary layer processes, such as horizontal rolls (Brooks and Rogers, 1997). A complete assesement of the variability of ϵ in different terrains would in fact improve our understanding of the main drivers which determine the development and dissipation of turbulence in various conditions. Once the variability of ϵ will be fully captured using different datasets, the
30 implementation of improvements to the turbulence parametrizations used in numerical models will be possible.

Data availability. The data of the sonic anemometers and wind Doppler lidars at the XPIA field campaign are publicly available at <https://a2e.energy.gov/data>.

Competing interests. The authors declare that they have no conflict of interest.

Acknowledgements. The authors thank Dr. Matthieu Boquet and Dr. Ludovic Thobois at Leosphere for providing the technical parameters of the WINDCUBE v1 and v2 needed for this analysis. We also appreciate Dr. Boquet's and Mr. Evan Osler's (Renewable NRG) efforts to provide the v2 to the XPIA field campaign. Support for JKL and NB is provided by the National Science Foundation (AGS-1554055) under
5 the CAREER program.

References

- Aitken, M. L., Rhodes, M. E., and Lundquist, J. K.: Performance of a wind-profiling lidar in the region of wind turbine rotor disks, *J. Atmos. Oceanic Technol.*, 29, 347–355, <https://doi.org/10.1175/JTECH-D-11-00033.1>, <http://dx.doi.org/10.1175/JTECH-D-11-00033.1>, 2012.
- Albertson, J. D., Parlange, M. B., Kiely, G., and Eichinger, W. E.: The average dissipation rate of turbulent kinetic energy in the neutral and unstable atmospheric surface layer, *Journal of Geophysical Research: Atmospheres*, 102, 13 423–13 432, 1997.
- 5 Babić, K., Bencetić Klaić, Z., and Večenaj, Ž.: Determining a turbulence averaging time scale by Fourier analysis for the nocturnal boundary layer, *Geofizika*, 29, 35–51, 2012.
- Baik, J.-J. and Kim, J.-J.: A numerical study of flow and pollutant dispersion characteristics in urban street canyons, *Journal of Applied Meteorology*, 38, 1576–1589, 1999.
- 10 Balsley, B., Frehlich, R., Jensen, M., and Meillier, Y.: High-resolution in situ profiling through the stable boundary layer: examination of the SBL top in terms of minimum shear, maximum stratification, and turbulence decrease, *Journal of the atmospheric sciences*, 63, 1291–1307, 2006.
- Banakh, V. and Smalikho, I.: Determination of the turbulent energy dissipation rate from lidar sensing data, *ATMOSPHERIC AND OCEANIC OPTICS C/C OF OPTIKA ATMOSFERI I OKEANA*, 10, 295–302, 1997.
- 15 Banakh, V., Werner, C., Köpp, F., and Smalikho, I.: Measurement of the turbulent energy dissipation rate with a scanning Doppler lidar, *ATMOSPHERIC AND OCEANIC OPTICS C/C OF OPTIKA ATMOSFERI I OKEANA*, 9, 849–853, 1996.
- Banakh, V. A., Smalikho, I. N., Köpp, F., and Werner, C.: Representativeness of wind measurements with a CW Doppler lidar in the atmospheric boundary layer, *Applied Optics*, 34, 2055–2067, 1995.
- Banta, R., Newsom, R., Lundquist, J., Pichugina, Y., Coulter, R., and Mahrt, L.: Nocturnal low-level jet characteristics over Kansas during CASES-99, *Boundary-Layer Meteorology*, 105, 221–252, 2002.
- 20 Banta, R. M., Pichugina, Y. L., and Brewer, W. A.: Turbulent velocity-variance profiles in the stable boundary layer generated by a nocturnal low-level jet, *Journal of the atmospheric sciences*, 63, 2700–2719, 2006.
- Barad, M. L.: Low-altitude jet streams, *Scientific American*, 205, 120–133, 1961.
- Brooks, I. M. and Rogers, D. P.: Aircraft observations of boundary layer rolls off the coast of California, *Journal of the Atmospheric Sciences*, 54, 1834–1849, 1997.
- 25 Brugger, P., Träumner, K., and Jung, C.: Evaluation of a procedure to correct spatial averaging in turbulence statistics from a Doppler lidar by comparing time series with an ultrasonic anemometer, *Journal of Atmospheric and Oceanic Technology*, 33, 2135–2144, 2016.
- Champagne, F., Friehe, C., LaRue, J., and Wynagaard, J.: Flux measurements, flux estimation techniques, and fine-scale turbulence measurements in the unstable surface layer over land, *Journal of the Atmospheric Sciences*, 34, 515–530, 1977.
- 30 Chapman, D. and Browning, K.: Measurements of dissipation rate in frontal zones, *Quarterly Journal of the Royal Meteorological Society*, 127, 1939–1959, 2001.
- Coen, J. L., Cameron, M., Michalakes, J., Patton, E. G., Riggan, P. J., and Yedinak, K. M.: WRF-Fire: coupled weather–wildland fire modeling with the weather research and forecasting model, *Journal of Applied Meteorology and Climatology*, 52, 16–38, 2013.
- Curtis, R. and Panofsky, H.: The relation between large-scale vertical motion and weather in summer, *Bulletin of the American Meteorological Society*, pp. 521–531, 1958.
- 35 De Franceschi, M. and Zardi, D.: Evaluation of cut-off frequency and correction of filter-induced phase lag and attenuation in eddy covariance analysis of turbulence data, *Boundary-Layer Meteorology*, 108, 289–303, 2003.

- Doviak, R. J. et al.: Doppler radar and weather observations, Courier Corporation, 1993.
- Drobinski, P., Dabas, A. M., and Flamant, P. H.: Remote measurement of turbulent wind spectra by heterodyne dopplerlidar technique, *Journal of Applied Meteorology*, 39, 2434–2451, 2000.
- Frehlich, R.: Coherent Doppler lidar signal covariance including wind shear and wind turbulence, *Applied Optics*, 33, 6472–6481, 1994.
- 5 Frehlich, R.: Estimation of velocity error for Doppler lidar measurements, *Journal of Atmospheric and Oceanic Technology*, 18, 1628–1639, 2001.
- Frehlich, R. and Sharman, R.: Estimates of turbulence from numerical weather prediction model output with applications to turbulence diagnosis and data assimilation, *Monthly Weather Review*, 132, 2308–2324, 2004.
- Frehlich, R., Meillier, Y., Jensen, M. L., Balsley, B., and Sharman, R.: Measurements of boundary layer profiles in an urban environment, *Journal of Applied Meteorology and Climatology*, 45, 821–837, 2006.
- 10 Gerz, T., Holzäpfel, F., Bryant, W., Köpp, F., Frech, M., Tafferner, A., and Winkelmann, G.: Research towards a wake-vortex advisory system for optimal aircraft spacing, *Comptes Rendus Physique*, 6, 501–523, 2005.
- Grell, G. A., Dudhia, J., Stauffer, D. R., et al.: A description of the fifth-generation Penn State/NCAR mesoscale model (MM5), 1994.
- Hong, S.-Y. and Dudhia, J.: Next-generation numerical weather prediction: Bridging parameterization, explicit clouds, and large eddies, *Bulletin of the American Meteorological Society*, 93, ES6–ES9, 2012.
- 15 Huang, K., Fu, J. S., Hsu, N. C., Gao, Y., Dong, X., Tsay, S.-C., and Lam, Y. F.: Impact assessment of biomass burning on air quality in Southeast and East Asia during BASE-ASIA, *Atmospheric Environment*, 78, 291–302, 2013.
- Kaimal, J. and Gaynor, J.: The boulder atmospheric observatory, *Journal of Climate and Applied Meteorology*, 22, 863–880, 1983.
- Kaimal, J. C., Wyngaard, J., Izumi, Y., and Coté, O.: Spectral characteristics of surface-layer turbulence, *Quarterly Journal of the Royal Meteorological Society*, 98, 563–589, 1972.
- 20 Kelley, N. D., Jonkman, B., and Scott, G.: Great Plains Turbulence Environment: Its Origins, Impact, and Simulation, Tech. rep., National Renewable Energy Laboratory (NREL), Golden, CO., 2006.
- Kolmogorov, A. N.: Dissipation of energy in locally isotropic turbulence, in: *Dokl. Akad. Nauk SSSR*, vol. 32, pp. 16–18, 1941.
- Kristensen, L., Lenschow, D., Kirkegaard, P., and Courtney, M.: The spectral velocity tensor for homogeneous boundary-layer turbulence, *in: Boundary Layer Studies and Applications*, pp. 149–193, Springer, 1989.
- 25 in: *Boundary Layer Studies and Applications*, pp. 149–193, Springer, 1989.
- Lenschow, D., Mann, J., and Kristensen, L.: How long is long enough when measuring fluxes and other turbulence statistics?, *Journal of Atmospheric and Oceanic Technology*, 11, 661–673, 1994.
- Lenschow, D. H., Wulfmeyer, V., and Senff, C.: Measuring second-through fourth-order moments in noisy data, *Journal of Atmospheric and Oceanic Technology*, 17, 1330–1347, 2000.
- 30 Lothon, M., Lenschow, D. H., and Mayor, S. D.: Doppler lidar measurements of vertical velocity spectra in the convective planetary boundary layer, *Boundary-layer meteorology*, 132, 205–226, 2009.
- Lundquist, J. K. and Bariteau, L.: Dissipation of Turbulence in the Wake of a Wind Turbine, *Boundary-Layer Meteorol*, 154, 229–241, <https://doi.org/10.1007/s10546-014-9978-3>, <http://link.springer.com/article/10.1007/s10546-014-9978-3>, 2014.
- Lundquist, J. K. and Chan, S. T.: Consequences of urban stability conditions for computational fluid dynamics simulations of urban dispersion, *Journal of applied meteorology and climatology*, 46, 1080–1097, 2007.
- 35 Lundquist, J. K., Wilczak, J. M., Ashton, R., Bianco, L., Brewer, W. A., Choukulkar, A., Clifton, A., Debnath, M., Delgado, R., Friedrich, K., et al.: Assessing state-of-the-art capabilities for probing the atmospheric boundary layer: the XPIA field campaign, *Bulletin of the American Meteorological Society*, 98, 289–314, 2017.

- Mann, J.: The spatial structure of neutral atmospheric surface-layer turbulence, *Journal of fluid mechanics*, 273, 141–168, 1994.
- McCaffrey, K., Bianco, L., and Wilczak, J. M.: Improved observations of turbulence dissipation rates from wind profiling radars, *Atmospheric Measurement Techniques*, 10, 2595–2611, <https://doi.org/10.5194/amt-10-2595-2017>, 2017a.
- McCaffrey, K., Quelet, P. T., Choukulkar, A., Wilczak, J. M., Wolfe, D. E., Oncley, S. P., Brewer, W. A., Debnath, M., Ashton, R., Iungo, G. V.,
5 et al.: Identification of tower-wake distortions using sonic anemometer and lidar measurements, *Atmospheric Measurement Techniques*, 10, 393, 2017b.
- Mirocha, J., Lundquist, J., and Kosović, B.: Implementation of a nonlinear subfilter turbulence stress model for large-eddy simulation in the Advanced Research WRF model, *Monthly Weather Review*, 138, 4212–4228, 2010.
- Muñoz-Esparza, D., Sharman, R. D., and Lundquist, J. K.: Turbulent dissipation rate in the atmospheric boundary layer: observations and
10 WRF mesoscale modeling during the XPIA field campaign, *Monthly Weather Review*, 2017.
- Muñoz-Esparza, D., Cañadillas, B., Neumann, T., and van Beeck, J.: Turbulent fluxes, stability and shear in the offshore environment: Mesoscale modelling and field observations at FINO1, *Journal of Renewable and Sustainable Energy*, 4, 063 136, <https://doi.org/10.1063/1.4769201>, 2012.
- Nakanishi, M. and Niino, H.: An improved Mellor–Yamada level-3 model: Its numerical stability and application to a regional prediction of
15 advection fog, *Boundary-Layer Meteorology*, 119, 397–407, 2006.
- Nakanishi, M. and Niino, H.: Development of an improved turbulence closure model for the atmospheric boundary layer, *Journal of the Meteorological Society of Japan. Ser. II*, 87, 895–912, 2009.
- Newsom, R. K., Brewer, W. A., Wilczak, J. M., Wolfe, D. E., Oncley, S. P., and Lundquist, J. K.: Validating precision estimates in horizontal wind measurements from a Doppler lidar, *Atmospheric Measurement Techniques*, 10, 1229, 2017.
- 20 Nilsson, E., Lohou, F., Lothon, M., Pardyjak, E., Mahrt, L., and Darbieu, C.: Turbulence kinetic energy budget during the afternoon transition–Part 1: Observed surface TKE budget and boundary layer description for 10 intensive observation period days, *Atmospheric Chemistry and Physics*, 16, 8849–8872, 2016.
- O’Connor, E. J., Illingworth, A. J., Brooks, I. M., Westbrook, C. D., Hogan, R. J., Davies, F., and Brooks, B. J.: A method for estimating the turbulent kinetic energy dissipation rate from a vertically pointing Doppler lidar, and independent evaluation from balloon-borne in situ
25 measurements, *Journal of Atmospheric and Oceanic Technology*, 27, 1652–1664, 2010.
- Olesen, H. R., Larsen, S. E., and Højstrup, J.: Modelling velocity spectra in the lower part of the planetary boundary layer, *Boundary-Layer Meteorology*, 29, 285–312, 1984.
- Oncley, S. P., Friehe, C. A., Larue, J. C., Businger, J. A., Itsweire, E. C., and Chang, S. S.: Surface-layer fluxes, profiles, and turbulence measurements over uniform terrain under near-neutral conditions, *Journal of the Atmospheric Sciences*, 53, 1029–1044, 1996.
- 30 Panofsky, H. A.: Matching in the convective planetary boundary layer, *Journal of the Atmospheric Sciences*, 35, 272–276, 1978.
- Paquin, J. and Pond, S.: The determination of the Kolmogoroff constants for velocity, temperature and humidity fluctuations from second- and third-order structure functions, *Journal of Fluid Mechanics*, 50, 257–269, 1971.
- Pearson, G., Davies, F., and Collier, C.: An analysis of the performance of the UFAM pulsed Doppler lidar for observing the boundary layer, *Journal of Atmospheric and Oceanic Technology*, 26, 240–250, 2009.
- 35 Piper, M. and Lundquist, J. K.: Surface layer turbulence measurements during a frontal passage, *Journal of the Atmospheric Sciences*, 61, 1768–1780, 2004.
- Prabha, T. V., Leclerc, M. Y., Karipot, A., and Hollinger, D. Y.: Low-frequency effects on eddy covariance fluxes under the influence of a low-level jet, *Journal of Applied Meteorology and Climatology*, 46, 338–352, 2007.

- Rhodes, M. E. and Lundquist, J. K.: The Effect of Wind-Turbine Wakes on Summertime US Midwest Atmospheric Wind Profiles as Observed with Ground-Based Doppler Lidar, *Boundary-Layer Meteorology*, 149, 85–103, <https://doi.org/10.1007/s10546-013-9834-x>, 2013.
- Rye, B.: Antenna parameters for incoherent backscatter heterodyne lidar, *Applied Optics*, 18, 1390–1398, 1979.
- Skamarock, W. C., Klemp, J. B., Dudhia, J., Gill, D. O., Barker, D. M., Wang, W., and Powers, J. G.: A description of the advanced research WRF version 2, Tech. rep., National Center For Atmospheric Research Boulder Co Mesoscale and Microscale Meteorology Div, 2005.
- Smalikho, I.: On measurement of the dissipation rate of the turbulent energy with a cw Doppler lidar, *ATMOSPHERIC AND OCEANIC OPTICS C/C OF OPTIKA ATMOSFERY I OKEANA*, 8, 788–793, 1995.
- Smalikho, I., Köpp, F., and Rahm, S.: Measurement of atmospheric turbulence by 2- μ m Doppler lidar, *Journal of Atmospheric and Oceanic Technology*, 22, 1733–1747, 2005.
- Smalikho, I. N. and Banakh, V. A.: Measurements of wind turbulence parameters by a conically scanning coherent Doppler lidar in the atmospheric boundary layer, *Atmospheric Measurement Techniques*, 10, 4191, 2017.
- Sobel, A. H. and Neelin, J. D.: The boundary layer contribution to intertropical convergence zones in the quasi-equilibrium tropical circulation model framework, *Theoretical and Computational Fluid Dynamics*, 20, 323–350, 2006.
- Sreenivasan, K. R.: On the universality of the Kolmogorov constant, *Physics of Fluids*, 7, 2778–2784, 1995.
- Taylor, G. I.: Statistical theory of turbulence, in: *Proceedings of the Royal Society of London A: Mathematical, Physical and Engineering Sciences*, vol. 151, pp. 421–444, The Royal Society, 1935.
- Tennekes, H. and Lumley, J. L.: *A first course in turbulence*, MIT press, Cambridge, MA, 1972.
- Tonttila, J., O'Connor, E., Hellsten, A., Hirsikko, A., O'Dowd, C., Järvinen, H., and Räisänen, P.: Turbulent structure and scaling of the inertial subrange in a stratocumulus-topped boundary layer observed by a Doppler lidar, *Atmospheric chemistry and physics*, 15, 5873–5885, 2015.
- Vanderwende, B. J., Lundquist, J. K., Rhodes, M. E., Takle, E. S., and Irvin, S. L.: Observing and simulating the summertime low-level jet in central Iowa, *Monthly Weather Review*, 143, 2319–2336, 2015.
- Wang, H., Barthelmie, R. J., Doubrawa, P., and Pryor, S. C.: Errors in radial velocity variance from Doppler wind lidar, *Atmospheric Measurement Techniques*, 9, 4123, 2016.
- Wharton, S. and Lundquist, J. K.: Assessing atmospheric stability and its impacts on rotor-disk wind characteristics at an onshore wind farm, *Wind Energy*, 15, 525–546, 2012.
- Wilczak, J. M., Oncley, S. P., and Stage, S. A.: Sonic anemometer tilt correction algorithms, *Boundary-Layer Meteorology*, 99, 127–150, 2001.
- Yang, B., Qian, Y., Berg, L. K., Ma, P.-L., Wharton, S., Bulaevskaya, V., Yan, H., Hou, Z., and Shaw, W. J.: Sensitivity of turbine-height wind speeds to parameters in planetary boundary-layer and surface-layer schemes in the weather research and forecasting model, *Boundary-Layer Meteorology*, 162, 117–142, 2017.
- Zhang, J. A., Drennan, W. M., Black, P. G., and French, J. R.: Turbulence structure of the hurricane boundary layer between the outer rainbands, *Journal of the Atmospheric Sciences*, 66, 2455–2467, 2009.

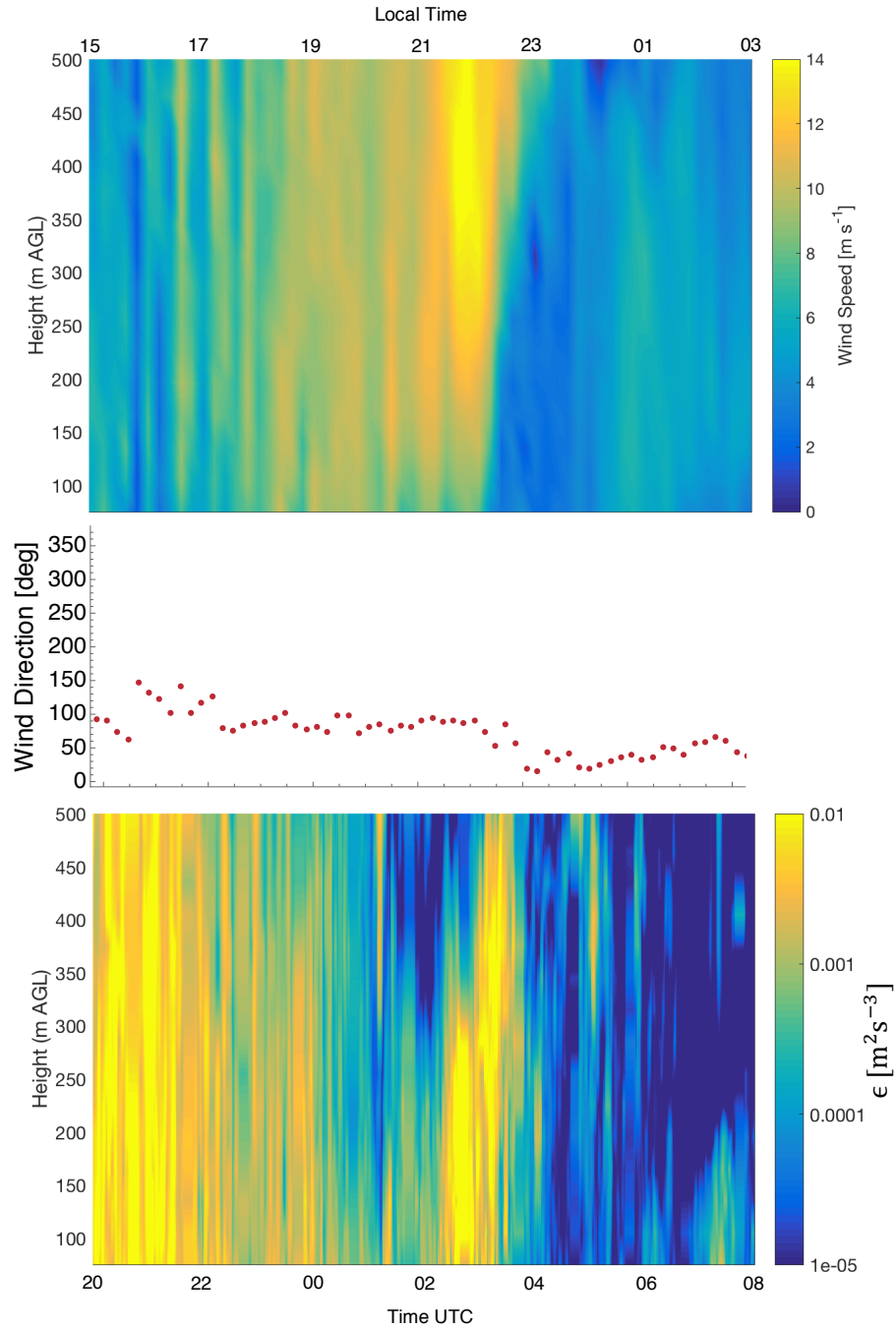


Figure 15. Nocturnal low-level jet case study. (a) Variability of wind speed from 20 UTC, 6 April 2015, to 8 UTC, 7 April 2015, as measured by the Halo Streamline lidar. (b) Wind direction at 116m AGL, during the same period of time. (c) Correspondent variability of turbulence dissipation rate ϵ as derived from the Halo Streamline measurements.